

Cooperative motor action to regulate microtubule length dynamics

Atul Kumar Verma, Natasha Sharma, and Arvind Kumar Gupta*

Department of Mathematics, Indian Institute of Technology Ropar, Rupnagar-140001, Punjab, India



(Received 6 July 2018; revised manuscript received 11 January 2019; published 7 March 2019)

Motivated by the recent experimental observations on motor induced cooperative mechanism controlling the length dynamics of microtubules (MTs), we examine how plus-end-targeted proteins of the kinesin family regulate MT polymerization and depolymerization routines. Here, we study a stochastic mathematical model capturing the unusual form of collective motor interaction on MT dynamics originating due to the molecular traffic near the MT tip. We provide an extensive analysis of the joint effect of motor impelled MT polymerization and complete depolymerization. The effect of the cooperative action is included by modifying the intrinsic depolymerization rate. We analyze the model within the framework of continuum mean-field theory and the resultant steady-state analytic solution is expressed in terms of Lambert W functions. Four distinct steady-state phases including a shock phase have been reported. The significant features of the shock including its position and height have been analyzed. Theoretical outcomes are supported by extensive Monte Carlo simulations. To explore the system alterations between the regime of growth and shrinkage phase, we consider kymographs of the microtubule along with the length distributions. Finally, we investigated the dependence of MT length kinetics both on modifying factor of depolymerization rate and motor concentration. The overall extensive study reveals that the flux of molecular traffic at the microtubule plus end initiates a cooperative mechanism, resulting in significant change in MT growth and shrinkage regime as also observed experimentally.

DOI: [10.1103/PhysRevE.99.032411](https://doi.org/10.1103/PhysRevE.99.032411)

I. INTRODUCTION AND BACKGROUND

Cells being the underlying units of living organisms are often called the “building blocks of life.” They are capable to carry out specialized functions including movement of substances across the cell membrane, cell division, and protein synthesis [1]. These functions depend on progressive microscopic processes and are robustly out of equilibrium due to a continuous supply of energy. The efficient delivery of critical cargoes to specific locations is essential for many cellular functions and occurs essentially in all eukaryotic cells [2]. The cytoskeleton network, comprising of microtubule (MT) filaments, plays a vital role in cellular trafficking. It aids as a road map for several kinds of mobile biological nanomachines, namely, the cytoskeletal motors such as kinesin, dynein, and myosin to walk along the filaments while carrying intracellular cargo vesicles from the site of supply to the site of demand [3–7]. Along with directed motion, due to finite processivity, molecular motors can detach from the filament to the surroundings and diffusing motors from the vicinity can also approach and attach to a site of the filament [8].

Microtubule, a type of cytoskeletal filament, is an intracellular structure that determines cell shapes and controls various kinds of essential movements in cells including mitosis [9], cytokinesis [10], and intracellular transport [11]. These are polymers with basic subunits α/β -tubulin of 8-nm length, that spontaneously gather along with their long axis into a microtubule of relatively 25 nm of diameter [12]. Generally,

12–14 of these protofilaments wrap into a helical cylinder known as a microtubule. The dissimilarity of the α - β dimer subunit results in two structurally distinct ends of MT: the plus end and the minus end [13].

Structurally, MTs are the stiffest component of the cytoskeleton network displaying a complex dynamic instability, featured by a stochastic swapping within phases of continuous growth (polymerization) or rapid shrinkage (depolymerization) [14–16]. MTs grow and shrink with different kinetic rates for both polymerization and depolymerization dynamics from plus and minus end simultaneously [17]. Since microtubules are engrossed in a wide variety of requisite cellular operations, proper microtubule length regulation by certain cellular mechanisms is essential to expedite these tasks. Several *in vitro* and *in vivo* investigations and experiments reveal that these mechanisms are strongly influenced by complex actions including guanosine triphosphate (GTP) hydrolysis [15,18], mechanical forces [19], and microtubule associated proteins [20]. Regulation of such actions probably controls the length dynamics of the microtubules.

One of the characterized cellular factors that regulate MT dynamics is different molecular motors and various families of MT-associated proteins [21]. Among these, motors in the kinesin-8 family (Kip3p) strongly influence the MT polymerization dynamics and are crucial regulators of its length kinetics [20]. In general, it is observed that kinesin-8 restrain MT growth by inducing switching of MTs from growth to shrinkage phase [22]. After attaching strongly at a random site on a microtubule, being highly processive plus-end (tip) directed motor, the proteins proceed toward the plus end and exhibit a long run length. Recent experiments [20,22] and theoretical work [23] revealed their tip depolymerization

*akgupta@iitrpr.ac.in

action accomplished by the stacking of motors along the MT. The significant outcome of these studies is that the longer MTs depolymerize rapidly in comparison to shorter ones, featuring a length-dependent activity. A parallel length-dependent control of MT dynamics by kinesin-5 motors have been noted in *in vivo* analysis [24]. This length-dependent depolymerization along with polymerization leads to microtubule length control.

To understand the biological relevance of molecular mechanisms on MTs and to examine the transport phenomena, a paradigmatic model, namely, totally asymmetric simple exclusion process (TASEP) [25], has become a classical model for studying self-driven out-of-equilibrium systems. TASEP models have been extensively used to study a large number of biological and physical systems, ranging from intracellular transport and gene transcription to vehicular and pedestrian dynamics [26]. Despite their simplicity, TASEPs have successfully revealed a number of complex nonequilibrium phenomena [27–29]. It is a stochastic model considering particle movement along “tracks” or “trails.” These tracks are mimicked by a one-dimensional lattice, on which particles progress in preferred direction obeying a hard-core exclusion principle with a certain preassigned set of rules. The particles enter the lattice at one end and unless obstructed by other particles, they hop toward the opposite end and, eventually, leave the lattice. In addition, particles can attach and detach to and from the lattice at bulk sites [Langmuir kinetics (LK)] [30]. A few TASEP based studies have been conducted to understand the regulatory mechanisms of length control including the interplay between the polymerization kinetics and motor induced depolymerization. In this direction, several extensions of single lane exclusion processes with particle induced polymerization coupled with LK and without LK has been studied extensively [23,31–36]. Klein *et al.* [37] investigated a single lane exclusion process considering both sided hopping rules along with depolymerization. The study revealed that under certain conditions, motors dynamically accumulate at the filament ends. Later, a single lane TASEP with LK has been investigated to visualize the interplay between both MT polymerization and depolymerization [38,39]. In the context of MT dynamics at both the ends, Johann *et al.* [40] proposed a single lane TASEP-LK model with polymerization and depolymerization at different ends to study the effect of the motor-induced depolymerization. Further, few researchers have also studied length regulation under processive (non-processive) depolymerization with bidirectional hopping rules [41,42].

Interestingly, the leading *in vivo* and *in vitro* experimental studies of Kip3p proteins highlighted a surprising finding [20,22]. It suggested that the motors act cooperatively to induce length-dependent MT depolymerization. When an individual Kip3p molecule reaches unoccupied MT tip, it stands there for around half a minute. During this time, Kip3p molecule removes terminal dimer partially and then stays bounded until a neighboring Kip3p molecule from back knocks it down, resulting in complete tip removal. This cooperative interaction leads to a depolymerization rate that is proportional to the number of motors near to the microtubule end and is liable for the length dependence of depolymerization. In contrast to prior theoretical models, our model incorporates

more realistic cooperative motor actions. In this work, we will show that this affects system dynamics significantly and is essential for the regulation of MT length dynamics under polymerization and flux-dependent depolymerization [22].

Besides, our model is different than those studied in the past as following. In [23,37], polymerization is not considered while in [32] depolymerization is not taken up. Similarly, many studies [31,35,36,38–40] have considered spontaneous or inhibition polymerization with or without depolymerization. But, due to the lack of experimental knowledge on polymerization process in the presence of kinesin-8 at MT tip, past theoretical studies have hypothesized this process [38]. Therefore, we have adopted particle induced polymerization with depolymerization to fill this gap and to visualize if we can obtain any new physics. Moreover, none of the past studies [23,31–42] have considered cooperative motor action which eventually leads to flux-dependent depolymerization with polymerization, thereby making the proposed work more general in comparison to similar studies in the past.

Motivated by an unusual form of motor action to collectively cut back the length of the microtubule, as a first step in the direction, we formulated a TASEP based molecular mechanism considering the effect of cooperative interactions originating due to the molecular traffic near the plus end on MT dynamics. Notably, we have not considered the dynamics at the minus end as their rates are very small in comparison to those at the plus end [43]. We have especially examined the joint effect of motor stimulated MT polymerization, where MT growth is possible if the motor at the MT tip disassociates from the filament and complete depolymerization induced by collective motors on MT dynamics. The effect of cooperative interactions is examined by modifying the depolymerization rate based on the configuration of nearest neighboring sites [20,22]. It is significant to mention here that primarily to examine the cooperative motor action to regulate MT length alteration, we ignore spontaneous polymerization and depolymerization at this stage. This proposal enables us to study the impact of interactions on the complex dynamical processes including rich dynamics of MT length. The key motive is to analytically explore the qualitative as well as quantitative control of interactions on the length dynamics. The proposed framework gives some insight not only in understanding how collective motors can affect and control MT length, but also toward the enhancement of one’s insight into various nonequilibrium systems present in nature.

The paper is organized as follows. The model with all the relevant parameters is defined in Sec. II. Further, the mean-field framework is presented in Sec. III. Several results and discussions on significant parameters including phase diagrams, shock dynamics, and microtubule length dynamics based on theoretical and simulation studies are provided in Sec. IV. Finally, the results along with the future scope of the proposed system are summarized in Sec. V.

II. MINIMAL MODEL

We characterize the biological trails network as lattices: α - β dimer subunit as a site and plus-end-directed proteins moving along these lattices as particles. In particular, assuming individual protofilament of a MT as an independent

and noninteracting entity, we represent a protofilament as a semi-infinite one-dimensional lattice of length L with N sites, labeled $i = 1, \dots, N$, as depicted in Fig. 1. Here, on account of dynamic length behavior of MT, N is not constant and the lattice spacing $\epsilon = L/N$, length of a tubulin dimer (≈ 8.4 nm), is defined in such a way that it remains fixed for any value of N and L . The particles are distributed under the hard-core exclusion principle, which means that each lattice site can be either empty or occupied by exactly one particle. The state of the system is characterized by a set of occupation numbers, which indicate the spatial accumulation of the particles on the lattice. Distinctively, τ_i ($i = 1, 2, 3, \dots, N$) corresponds to the occupation number of a particle at i th lattice site, taking values $\tau_i = 0$ for empty and $\tau_i = 1$ for occupied site. For each time step, a lattice site i is randomly chosen and particle hopping takes place with a constant rate v (corresponding to relative 6.35 steps per second as from experimental data [22]), as per random-sequential update rules. The dynamical behavior of the defined system can be expressed in terms of the progression permitted for the particles according to the following dynamical rules.

(i) At boundary on the right ($i = N$), denoted by minus end, particles are injected into the lattice with a rate α provided $\tau_N = 0$. If $\tau_N = 1$ and $\tau_{N-1} = 0$, then the particle moves from site N to site $N - 1$ with a rate v . If $\tau_N = 1$ and $\tau_{N-1} = 1$, no hopping occurs from the right boundary.

(ii) For $1 < i < N$, the particles symmetrically hop to adjacent empty site from right to left at rate v , and interact via hard-core repulsion. Along with directed motion, we additionally consider the interaction of particles with surroundings through LK process. Molecular motors present at a constant concentration c are assumed to randomly attach from the surrounding environment to empty lattice site with a rate $c\omega_a$. Once attached, these motors move toward the plus end with the same hopping rate v . Additionally, the particle at the i th site ($i = 2, 3, \dots, N - 1$) can also detach with a rate ω_d , independent of c .

(iii) At boundary on the left ($i = 1$), referred as plus end, we consider MT dynamics that originate due to the interaction of molecular motors with the plus-end tip. When a particle progressing toward left from right reaches the tip, MT polymerizes with rate γ , and the particle detaches from the lattice [32] [Fig. 1(a)]. It is important to mention here that due to lack of sufficient experimental knowledge on polymerization process in the presence of kinesin-8, past theoretical studies in the framework of TASEP have hypothesized this process [38]. But, experimental studies suggest that another motor from kinesin family, namely kinesin-5, promotes the polymerization and two different motors from a same group may behave in a similar way [44]. Besides, past studies have mainly focused on spontaneous polymerization, therefore, inspired by these facts, we have chosen particle induced polymerization for the sake of filling this gap and to observe its effect on the system dynamics. Further, motivated by recent experiments on cooperative depolymerization act [20,22], we assume that when a motor arrives at the MT tip, it binds stably to the terminal dimer [Fig. 1(c)] and stands there until an incoming particle bumps into this paused molecule. This leads to the complete dissociation of both the terminal dimer and motor with an accelerated rate $\delta^l \omega_D$ [Fig. 1(b)], resulting in shrinkage of the lattice. We incorporated the observed collective dynamics in the proposed mathematical system using parameter l which depends on the configuration of the nearest neighboring sites. Here, l is a positive integer representing the strength of the modifying factor $\delta > 1$ of intrinsic noncooperative depolymerization rate ω_D . The modified depolymerization dynamics at the occupied MT tip takes into account the configuration of two nearest neighboring sites according to the following rules:

- (1) If the site adjacent to the tip is empty, complete removal of the plus-end tip is not possible due to lack of direct interaction, as evidenced from the experiments [22], resulting in absence of depolymerization [Fig. 1(c)].
- (2) If $\tau_2 = 1$ and $\tau_3 = 0$, l takes the value 1 and complete depolymerization is triggered. For this scenario,

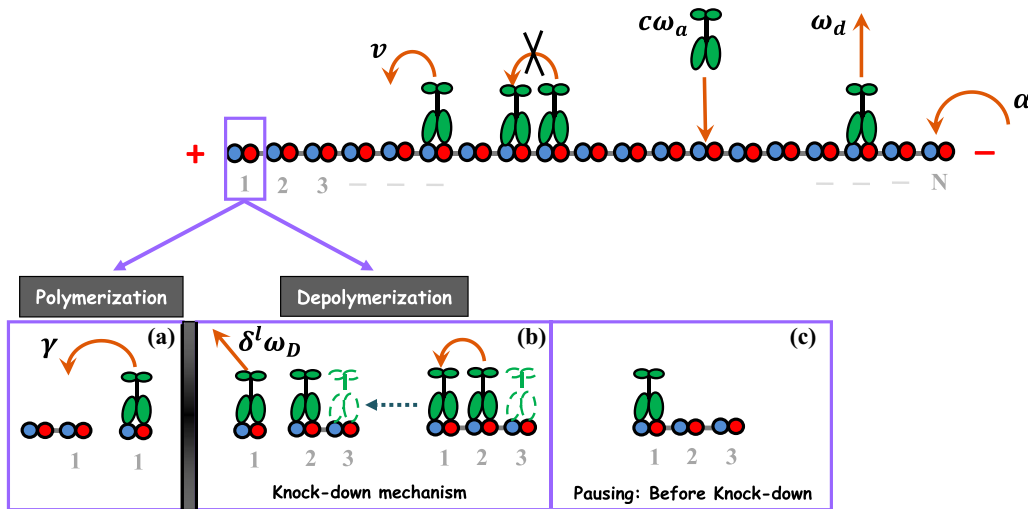


FIG. 1. Schematic representation of the model. Allowed transitions are shown by arrows. Crossed arrows indicate impermissible transitions. (a) MT growth dynamics, (b) knockdown mechanism resulting in accelerated detachment of plus-end bound motor by incoming motors, (c) paused molecule before knockdown.

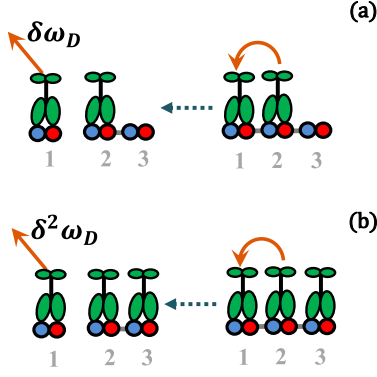


FIG. 2. Knockdown mechanism explaining the accelerated depolymerization dynamics at the occupied MT tip taking into account the configuration of (a) adjacent neighboring site, (b) two nearest neighboring sites.

noncooperative depolymerization rate ω_D is modified by a factor δ and the accelerated removal rate becomes $\delta\omega_D$ [Fig. 2(a)].

(3) If $\tau_2 = 1$ and $\tau_3 = 1$, modified depolymerization rate is adapted as $\delta^2\omega_D$ due to $l = 2$, as exhibited in Fig. 2(b).

The above mentioned dynamical rules are based on the *in vivo* and *in vitro* experiments for flux-dependent accelerated depolymerization [22] together with hypothesized particle induced polymerization [32]. Note that we have not considered the spontaneous polymerization and depolymerization, in particular, take place with a very slow rate, thereby, do not affect steady-state system dynamics significantly [22,32]. However, an extension of the presented model is possible on the similar lines by incorporating the remaining cases of polymerization and depolymerization processes in the absence of the motor at the tip and has been discussed in Appendix A. It has been found that the additional processes only increase the complexity of the model and do not affect the system dynamics qualitatively, which motivated us to ignore them in the further analysis and include them separately to avoid the lengthy calculations.

Besides, in the limiting case of $\omega_D = 0$ and $c = 1$, we retrieve the model studied in the literature [33]. The above considerations make the proposed model more general and realistic over the existing models [23,38] accounting for the interplay between MT dynamics and microtubule associated motors. It is notable to mention that in the following work, we consider $\nu = 1$ to set the basic timescale as proposed in the literature [33,38,39].

III. MEAN-FIELD ANALYSIS AND STEADY-STATE BEHAVIOR

Now, we analyze the proposed system obtained from the mean-field description and examine its behavior in the steady state. In this direction, we derive the resulting kinetic equations in terms of the mean site density for the evolution of occupancy of particles. Here, the stochastic processes defined above are included by considering the dynamics in a comoving frame with respect to plus-end tip. When the

polymerization takes place, the i th site label is updated by $(i + 1)th$, while for depolymerization it modifies to $(i - 1)th$. Thus, in case of lattice growth (shrinkage), the change in density at site i is the net result of particles entering from the site on the right (left), departing to the site on the left (right). For $i \geq 4$ (bulk of lattice), we obtain

$$\begin{aligned} \frac{d\langle\tau_i\rangle}{dt} &= \langle\tau_{i+1}(1 - \tau_i)\rangle - \langle\tau_i(1 - \tau_{i-1})\rangle + c\omega_a\langle 1 - \tau_i\rangle \\ &\quad - \omega_d\langle\tau_i\rangle + \gamma\langle\tau_i(\tau_{i-1} - \tau_i)\rangle \\ &\quad + \omega_D[\delta\langle\tau_1\tau_2(\tau_{i+1} - \tau_i)\rangle + \delta^2\langle\tau_1\tau_2\tau_3(\tau_{i+1} - \tau_i)\rangle], \end{aligned} \quad (1)$$

where $\langle \dots \rangle$ denotes the statistical average. Here, the first two terms on the right hand side represent forward hopping from right to left obeying hard-core exclusion principle. The third and fourth terms describe the corresponding gain and loss terms arising due to attachment and detachment processes. Capturing the interplay between the MT tip and motors, the last two terms corresponding to γ and ω_D exemplify the role of polymerization and depolymerization dynamics, respectively.

Further, due to the consideration of accelerated depolymerization on account of two nearest neighboring sites, second and third in particular, the particle density at the sites $i = 1, 2$, and 3 in the comoving frame of the tip can be computed as

$$\begin{aligned} \frac{d\langle\tau_1\rangle}{dt} &= \langle\tau_2(1 - \tau_1)\rangle - \gamma\langle\tau_1\rangle, \\ \frac{d\langle\tau_2\rangle}{dt} &= \langle\tau_3(1 - \tau_2)\rangle - \langle\tau_2(1 - \tau_1)\rangle - \gamma\langle\tau_1\tau_2\rangle \\ &\quad + c\omega_a\langle 1 - \tau_2\rangle - \omega_d\langle\tau_2\rangle + \delta\omega_D\langle\tau_1\tau_2\tau_3\rangle \\ &\quad - \delta\omega_D\langle\tau_1\tau_2\rangle, \\ \frac{d\langle\tau_3\rangle}{dt} &= \langle\tau_4(1 - \tau_3)\rangle - \langle\tau_3(1 - \tau_2)\rangle + \gamma\langle\tau_1\tau_2\rangle - \gamma\langle\tau_1\tau_3\rangle \\ &\quad + c\omega_a\langle 1 - \tau_3\rangle - \omega_d\langle\tau_3\rangle + \delta\omega_D\langle\tau_1\tau_2\tau_4\rangle \\ &\quad - \delta\omega_D\langle\tau_1\tau_2\tau_3\rangle + \delta^2\omega_D\langle\tau_1\tau_2\tau_3\tau_4\rangle - \delta^2\omega_D\langle\tau_1\tau_2\tau_3\rangle. \end{aligned} \quad (2)$$

At the fixed right end of the lattice, $i = N$, the occupancy of particles evolve according to

$$\frac{d\langle\tau_N\rangle}{dt} = \alpha\langle(1 - \tau_N)\rangle - \langle\tau_N(1 - \tau_{N-1})\rangle. \quad (3)$$

Ignoring particle spatial correlations and factorizing the corresponding correlation function as product of their averages, we have

$$\langle\tau_i\tau_j\rangle = \langle\tau_i\rangle\langle\tau_j\rangle. \quad (4)$$

For large system size $N \rightarrow \infty$ and small lattice constant $\epsilon = L/N \rightarrow 0$ with finite $N\epsilon$, we can derive the continuum limit by coarse graining a discrete lattice with continuous variable $x = iL/N$ and rescaling the time as $t' = tL/N$. For simplicity, we fix the length of the lattice as $L = 1$ restricting the variable x in the range $[0, 1]$. Since the nonconserving processes in the system occur at lower rates in comparison to particle conserving processes, the system attains steady state locally due to conservative dynamics only. Therefore, the

adopted time rescaling is useful to understand the engagement between particle conserving and nonconserving dynamics [45]. Besides, to observe competition between boundary and bulk dynamics, we rescale LK rates in such a way that the original rates decrease with an increase in system size N as proposed in the literature [46]. In this direction, we consider

$$\begin{aligned}\Omega_a &= \omega_a N, \\ \Omega_d &= \omega_d N.\end{aligned}\quad (5)$$

In the continuum limit, replacing $\langle \tau_i \rangle$ by a continuous variable $\rho_i \in [0, 1]$ and retaining the terms up to $O(N^{-2})$ in Taylor's series expansion we obtain

$$\rho_{i\pm 1} = \rho_i \pm \frac{1}{N} \frac{\partial \rho_i}{\partial x} + \frac{1}{2N^2} \frac{\partial^2 \rho_i^2}{\partial x^2} + O\left(\frac{1}{N^3}\right). \quad (6)$$

Without loss of generality, dropping subscript i as the system is free from any kind of spatial inhomogeneity and denoting t' by t , the continuum mean-field equation describing steady-state bulk densities can be given as

$$\frac{\partial \rho}{\partial t} = E \frac{\partial^2 \rho}{\partial x^2} + \frac{\partial J}{\partial x} - (c\Omega_a + \Omega_d)\rho + c\Omega_a, \quad (7)$$

where

$$E = \frac{\epsilon}{2} [1 + \gamma \rho_1 + \delta \omega_D \rho_1 \rho_2 (1 + \delta \rho_3)] \quad (8)$$

and

$$J = \rho(1 - \rho) - [\gamma \rho_1 - \delta \omega_D \rho_1 \rho_2 (1 + \delta \rho_3)]\rho. \quad (9)$$

Here, J is the bulk current in the lattice with respect to the comoving frame. Similarly, in the continuum limit the evolution equations of density at sites 1, 2, and 3 are given by

$$\begin{aligned}\frac{d\rho_1}{dt} &= \rho_2(1 - \rho_1) - \gamma \rho_1, \\ \frac{d\rho_2}{dt} &= \rho_3(1 - \rho_2) - \rho_2(1 - \rho_1) - \gamma \rho_1 \rho_2 + c\Omega_a(1 - \rho_2) \\ &\quad - \Omega_d \rho_2 + \delta \omega_D \rho_1 \rho_2 \rho_3 - \delta \omega_D \rho_1 \rho_2, \\ \frac{d\rho_3}{dt} &= \rho_4(1 - \rho_3) - \rho_3(1 - \rho_2) + \gamma \rho_1 \rho_2 - \gamma \rho_1 \rho_3 \\ &\quad + c\Omega_a(1 - \rho_3) - \Omega_d \rho_3 + \delta \omega_D \rho_1 \rho_2 \rho_4 - \delta \omega_D \rho_1 \rho_2 \rho_3 \\ &\quad + \delta^2 \omega_D \rho_1 \rho_2 \rho_3 \rho_4 - \delta^2 \omega_D \rho_1 \rho_2 \rho_3.\end{aligned}\quad (10)$$

Additionally, the density at the N th site evolves as

$$\frac{d\rho_N}{dt} = \alpha(1 - \rho_N) - \rho_N(1 - \rho_{N-1}). \quad (11)$$

In the limit of $\epsilon \rightarrow 0$, the continuum steady-state equation assumes the form

$$\frac{\partial \rho}{\partial x} = \frac{(c\Omega_a + \Omega_d)\rho - c\Omega_a}{1 - 2\rho - \gamma \rho_1 + \delta \omega_D \rho_1 \rho_2 (1 + \delta \rho_3)}, \quad (12)$$

where ρ_1 , ρ_2 , and ρ_3 can be obtained by solving the system in Eq. (10) in steady state taking an approximation $\rho_3 = \rho_4$. Due to the involved complexity in the above system, we first attempt to find an explicit solution for a special regime where

the various rates satisfy the condition

$$\frac{1 - \gamma \rho_1 + \delta \omega_D \rho_1 \rho_2 (1 + \delta \rho_3)}{2} = \frac{c\Omega_a}{c\Omega_a + \Omega_d}. \quad (13)$$

The assumption in Eq. (13) enables us to compute steady-state average density ρ explicitly in terms of x and other model parameters. For the above choice of constraints, the steady-state equation for the bulk reduces to

$$\left[\rho - \frac{c\Omega_a}{c\Omega_a + \Omega_d} \right] \left[\frac{d\rho}{dx} + B \right] = 0, \quad (14)$$

where $B = \frac{c\Omega_a + \Omega_d}{2}$.

The solution of the above equation leads to mean-field density profiles for the low density ($\rho < 0.5$) (LD), constant density (CD), and high density ($\rho > 0.5$) (HD) phases as

$$\rho(x) = \begin{cases} \rho_{\text{HD}}(x) = \rho_3 - Bx, \\ \rho_{\text{CD}}(x) = \frac{1 - \gamma \rho_1 + \delta \omega_D \rho_1 \rho_2 (1 + \delta \rho_3)}{2}, \\ \rho_{\text{LD}}(x) = \alpha + B(1 - x). \end{cases} \quad (15)$$

These mean-field expressions correspond to a linear solution for the case of the LD and HD phases and a homogeneous density profile for the case of the CD phase. Please see Appendix B for proof of the above solution.

Although simpler to analyze, the previous case in Eq. (13) is somewhat particular as it depends upon a specific set of parameters. Generally, one would not expect Eq. (13) to hold always. Alternatively, to analyze the system dynamics completely and to obtain full solution of Eq. (12), we derive its explicit solution which has been obtained in form of a special function, namely, Lambert W function [47]. In this direction, we consider a rescaled density in the form as follows:

$$\sigma(x) = \frac{-2\rho + \frac{2K}{K+1}}{\frac{-2K}{K+1} + [1 - \gamma \rho_1 + \delta \omega_D \rho_1 \rho_2 (1 + \delta \rho_3)]}, \quad (16)$$

where $K = c\Omega_a/\Omega_d$. Since the density $\rho(x)$ is restrained to the interval $[0, 1]$, the rescaled density $\sigma(x)$ can have values within the interval $[\frac{-2K}{H}, \frac{2}{H}]$, where $H = K - 1 + (1 + K)[\gamma \rho_1 - \delta \omega_D \rho_1 \rho_2 (1 + \delta \rho_3)]$. Clearly, H takes positive values for the adopted set of parameters. For the above transformation, Eq. (12) simplifies to

$$\partial_x \sigma(x) + \partial_x \ln |\sigma(x)| = -\frac{\Omega_d(K+1)^2}{H}. \quad (17)$$

Integrating Eq. (17) outturn (for details see Appendix C)

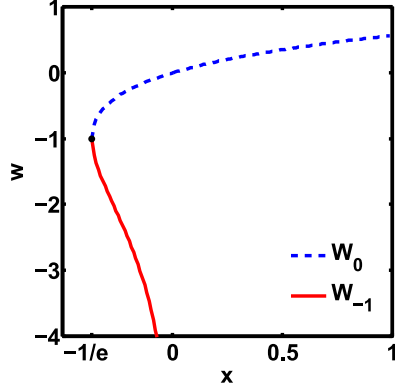
$$|\sigma(x)| \exp[\sigma(x)] = Y(x), \quad (18)$$

where $Y(x)$ is given by

$$Y(x) = |\sigma(x_0)| \exp \left[\sigma(x_0) - \frac{\Omega_d(K+1)^2}{H} (x - x_0) \right], \quad (19)$$

and $\sigma(x_0)$ is the value of the density as computed from Eq. (16) at the boundary point x_0 . In particular, $Y(x)$ that match the boundary condition on the left or right end of the system can be written as

$$Y_{\rho_3}(x) = |\sigma(0)| \exp \left[\sigma(0) - \frac{\Omega_d(K+1)^2}{H} x \right], \quad (20)$$


 FIG. 3. The real branches W_0 and W_{-1} of Lambert W function.

$$Y_\alpha(x) = |\sigma(1)| \exp \left[\sigma(1) - \frac{\Omega_d(K+1)^2}{H}(x-1) \right], \quad (21)$$

where $\sigma(0)$ and $\sigma(1)$ can be computed in terms of kinetic rates using Eq. (16) and boundary conditions $\rho(0) = \rho_3$ and $\rho(1) = \alpha$. As inferred from Eqs. (1) and (2), here $x = 0$ signifies the left boundary represented by third lattice site while $x = 1$ exhibits the right end of the lattice. Relations in Eq. (18) appear in various references such as population growth and hydrodynamics [47]. This type of equation has an explicit solution written in terms of a special function called Lambert W function [47] as

$$\begin{aligned} \sigma(x) &= W(Y(x)), & \sigma(x) > 0 \\ \sigma(x) &= W(-Y(x)), & \sigma(x) < 0. \end{aligned} \quad (22)$$

The Lambert W function is a multivalued function with two real branches (see Fig. 3), which we refer to as W_0 and W_{-1} . The branch of W is selected based on the rescaled density σ . For $\sigma \in [-\frac{2K}{H}, -1]$ the suitable solution is $W_{-1}(-Y)$, while for $\sigma \in [-1, 0]$ the relevant solution is obtained by $W_0(-Y)$. Eventually, for σ belonging to $[0, \frac{2}{H}]$, we have $W_0(Y)$.

The obtained solutions for the adopted parameters, using left and right boundary conditions, are given by

$$\begin{aligned} \rho_{HD}(x) &= \frac{1}{2} \left[\frac{2K}{K+1} [1 + W_0(-Y_{\rho_3}(x))] - W_0(-Y_{\rho_3}(x)) \right. \\ &\quad \left. \times [1 - \gamma \rho_1 + \delta \omega_D \rho_1 \rho_2 (1 + \delta \rho_3)] \right] \end{aligned} \quad (23)$$

and

$$\begin{aligned} \rho_{LD}(x) &= \frac{1}{2} \left[\frac{2K}{K+1} [1 + W_{-1}(-Y_\alpha(x))] - W_{-1}(-Y_\alpha(x)) \right. \\ &\quad \left. \times [1 - \gamma \rho_1 + \delta \omega_D \rho_1 \rho_2 (1 + \delta \rho_3)] \right]. \end{aligned} \quad (24)$$

Here, as mentioned, ρ_{LD} and ρ_{HD} denote the low and high density solutions obtained by right and left boundaries, respectively.

Additionally, to validate our theoretical findings, we have provided an alternative way to obtain the implicit solution of Eq. (12) in Appendix D.

TABLE I. Parameter values in experiment [22,23,38].

Parameter	Value
Dimer length [23]	8.4 nm
Hopping rate [22,38]	$v = 6.35 \text{ steps s}^{-1}$
Attachment rate [22,23,38]	$\omega_a = 24 \text{ (nM min } \mu\text{m)}^{-1}$
Detachment rate [23]	$\omega_d = 7.6 \times 10^{-4} \text{ s}^{-1}$
Concentration	$c \text{ in nM}$

IV. METHODS AND MATERIAL

The model parameters employed in the proposed work are based on the available *in vivo* and *in vitro* studies on motor transport in biological systems [22]. The details of parameters referred in experimental studies with their units are provided in Table I [22,23,38]. Besides, the parameters used in the theoretical model are summarized in Table II. Apart from certain disclosed specifications for transport mechanisms on the MT, the parameters detailing the polymerization rate $\gamma \in [0, 1]$ and the depolymerization rate $w_D \in [0, 1]$ are yet to be approximated from experiments [38]. Based on the underlying biological outcomes, the modifying factor $\delta > 1$ of intrinsic noncooperative depolymerization rate w_D is taken as 1.1 [22].

In order to validate our theoretical findings, we simultaneously developed a kinetic Monte Carlo simulation for the proposed model in Fig. 1. The simulated filament includes an array of binary numbers representing τ_i ($i = 1, \dots, N$). To sample the filament, at each time step, a site is chosen at random and a transition is attempted with the rates defined in Sec. II. One time step comprises of N such updates, so that, on an average, a lattice site is altered once per time stamp. Here, keeping our time unit constant, the number of updates per time step increases with increase in N . Note that during one time stamp the system may increase or decrease in length. As a consequence, if polymerization takes place, the i th site is updated as $(i+1)$ th site. Similarly, if the depolymerization occurs, the i th site transforms into $(i-1)$ th site and lattice shrinks by one site. In principle, this would affect our unit of time, however, such an increase or decrease, typically of one lattice unit, will be insignificant in the limit of $N \rightarrow \infty$.

Our desire is to allow the system to reach a steady state and calculate significant quantities including phase diagrams, density profiles, and lattice length distributions. A problem with the adopted simulation technique is that as $N \rightarrow \infty$,

TABLE II. Quantification of parameter values (unitless) used in the proposed model as obtained from similar studies in literature [22,23,38].

Parameter	Value
Hopping rate [38]	$v = 1$
Attachment rate [22,23]	$\Omega_a = 5.3 \times 10^{-4}$
Detachment rate [23]	$\Omega_d = 7.6 \times 10^{-4}$
Polymerization rate	$\gamma \in [0, 1]$
Depolymerization rate	$\omega_D \in [0, 1]$
Entry rate	$\alpha \in [0, 1]$
Modifying factor [22]	$\delta > 1$
Concentration	$c > 1$

computational cost increases. To minimize this problem, we have considered only a fixed length portion of the lattice in a comoving frame and simulations have been performed for 10^9 – 10^{10} time steps after ignoring initial 5% time steps. Also, the steady-state densities are calculated by averaging over an interval of $10N$ in the reference of the comoving frame of the tip.

V. RESULT AND DISCUSSIONS

A. Phase diagram and density profiles

To understand the steady-state behavior and further to explore the effect of the flux of molecular traffic on the system dynamics, we derive phase diagrams for a range of concentrations in the controlling parameter space (α, γ) . Figure 4 shows the composition of the phase plane, clearly indicating four distinct steady-state phases including low density (LD), high density (HD), mixed low-high (LH), and shock (S) phases. For the sake of clarity, we determine the expressions for the phase coexistence lines among the observed phases.

Phase coexistence line between LD and HD phases. This can be obtained by using the expressions of current J from Eq. (9) and equating the current for LD phase with the current for HD phase at $x = 1$, so that $J_{LD}(1) = J_{HD}(1)$. We thus have

$$\rho_{LD}(1)[1 - \rho_{LD}(1)] - \left(\frac{H+1-K}{K+1} \right) \rho_{LD}(1) = J_{HD}(1), \quad (25)$$

where $J_{HD}(1) = \rho_{HD}(1)[1 - \rho_{HD}(1)] - \left(\frac{H+1-K}{K+1} \right) \rho_{HD}(1)$.

Here, $\rho_{LD}(1)$ and $\rho_{HD}(1)$ are the densities at the right boundary in low and high density phases, respectively, and are obtained from Eqs. (16) and (22) with suitable Lambert W function branch as discussed in the previous section.

Phase boundary between LD and LH phases. We determined the phase boundary between low and low-high density phases by equating the current for LD phase with the current for HD phase at $x = 0$, i.e., $J_{LD}(0) = J_{HD}(0)$. Using the above condition, we have

$$\rho_{LD}(0)[1 - \rho_{LD}(0)] - \left(\frac{H+1-K}{K+1} \right) \rho_{LD}(0) = J_{HD}(0) \quad (26)$$

with $J_{HD}(0) = \rho_{HD}(0)[1 - \rho_{HD}(0)] - \left(\frac{H+1-K}{K+1} \right) \rho_{HD}(0)$. In particular, $\rho_{LD}(0)$ and $\rho_{HD}(0)$ are densities at left boundary in low and high density phases, respectively. Similarly, one can have the phase boundaries shared by S phase with LD and HD phases, respectively. It is to be noted that the location of the shock is determined by equating the obtained current for the LD and HD phases.

Distinctively, as evident from Fig. 4, the increasing concentrations show both qualitative as well as quantitative changes in the phase diagram. For significantly smaller values of concentrations, until $c_1 \approx 30$, three phases including LD, HD, and S phases are observed with dominating LD phase as displayed in Fig. 4(a). Physically, for higher values of polymerization rate, growth process accelerates resulting in the conversion of particles into empty sites. At this stage, along with the

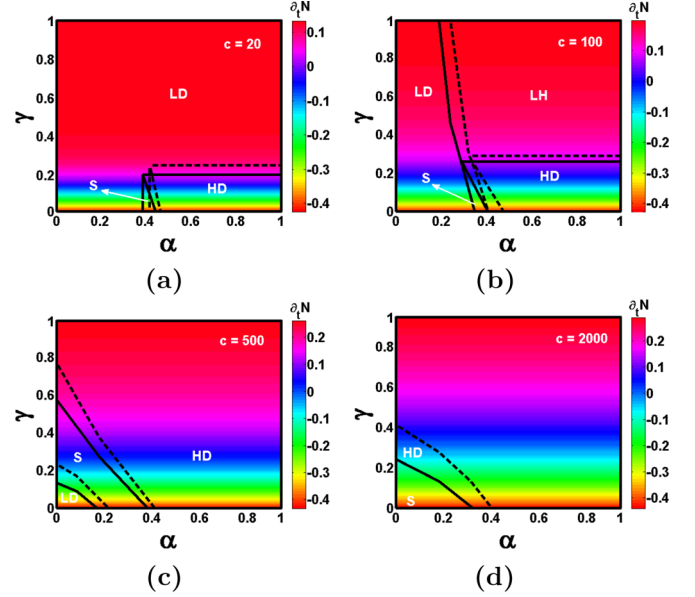


FIG. 4. Phase diagrams for varied c as (a) 20, (b) 100, (c) 500, (d) 2000 with $N = 1000$, $\omega_D = 0.2$, $\Omega_a = 5.3 \times 10^{-4}$, and $\Omega_d = 7.6 \times 10^{-4}$. Solid lines denote phase transition for $\delta = 1.1$, while dotted lines are those obtained for $\delta = 1.5$. Color code running from orange to red represents the transition from shrinkage to growth phase as calculated from Eq. (27) for $\delta = 1.1$.

prevailing scarcity of the particles in the system on account of low concentration, low density phase dominates. Prior to c_1 , no qualitative changes have been observed in the phase diagram except the repositioning of the phase boundaries due to enlargement and shrinkage of various existing phases. The LD phase shrinks, while the HD and S phases expand due to increase in motor concentration. With a further increase in c , beyond c_1 , along with the preexisting phases, one observes the emergence of new mixed LH phase in the locale of LD and HD phases. As an outcome of this, the shifting of the phase boundaries has been observed resulting in shrinkage of the LD phase and expansion of the HD phase. The noticed structural changes have been exhibited for $c = 100$ in Fig. 4(b). The appearance of the phase at this stage can be physically attributed to the increased number of particles attaching from the background to the lattice, resulting in some part of the bulk to be in low density while the remaining part to have high density. Besides, the observed continuous phase transitions from LD to HD phase is exhibited in Fig. 5(a). As evident from this figure that for a comparatively lower value of α , the LD profile emerges which converts into a shock with increase in entry rate. With further increment in α due to more particles on MT transition of shock phase into high density phase has been observed as shown in Fig. 5(a). Similarly, Fig. 5(b) displays the phase transition from the S phase to LH phase with respect to γ . Initially, for lower values of γ there is a shock phase which transits into a HD phase with an increase in γ . But, further increase in γ reduces the number of motors on MT due to particle induced polymerization leading to conversion of HD phase into LH phase. No significant change is observed in the phase diagram until $c_2 \approx 220$ at which the mixed LH phase ceases to exist. With more increase in concentrations,

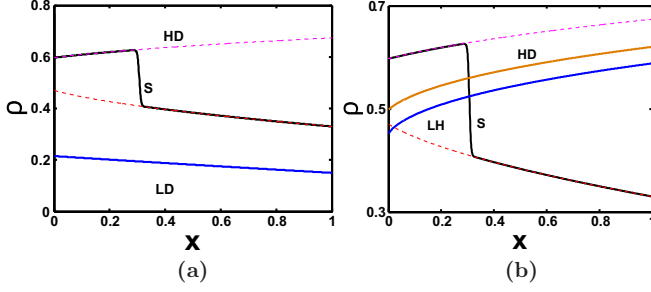


FIG. 5. Phase transitions from (a) low density (LD) to high density (HD) phase for $\gamma = 0.18$ with varied α as 0.15, 0.33, and 0.55, (b) S to LH phase for $\alpha = 0.33$ with varied $\gamma = 0.18, 0.26$, and 0.40. These values are for curves from bottom to top in (a) with $N = 1000$, $\omega_D = 0.20$, $c = 100$, $\Omega_a = 5.3 \times 10^{-4}$, $\Omega_d = 7.6 \times 10^{-4}$, and $\delta = 1.1$. In (b) other parameters are same as for (a) but dashed red and pink color curves are for $\gamma = 0.18$ while solid yellow and blue color are for $\gamma = 0.26$ and 0.40 , respectively. Shock profile in both (a) and (b) shown in black color is obtained by solving Eq. (7) numerically and all other profiles are obtained using a suitable branch of Lambert W function as discussed in Sec. III.

as expected due to the abundance of particles on the lattice, the region containing LD phase contracts, while the region of HD and S phases expands [see Fig. 4(c)]. Afar $c_3 \approx 750$, the LD phase disappears, altering the phase boundaries due to expansion and shrinkage of the existing phases. The phase diagram for $c = 2000$, capturing the above noticed changes more apparently, is shown in Fig. 4(d). The topology of the phase diagram remains preserved for further values of c up to 12 000 except transitions in domain boundaries beyond which S phase disappears. Note that the HD (LD) phase expands (shrinks) monotonically, while the region of S and LH phase exhibits nonmonotonic behavior with respect to increasing c .

Moreover, the alteration in concentrations has generated notable differences in the regime of growth and shrinkage phase. Precisely, as already noted in the previous section, a mean-field description of the length change of the MT is determined by

$$\frac{\partial N}{\partial t} = \gamma \rho_1 - \delta \omega_D \rho_1 \rho_2 - \delta^2 \omega_D \rho_1 \rho_2 \rho_3. \quad (27)$$

Here, the first term on the right hand side contributes as a gain term which is responsible for lattice growth, while the remaining terms representing the loss account for the lattice shrinkage. Figures 4(a)–4(d) display the region of MT shrinkage and growth with varied c by means of a color code running from orange (shrinkage) to red (growth) representing the increase in MT length for $\delta = 1.1$. As expected, the increase in concentrations extends the MT shrinkage region, revealing an interesting outcome of accelerated depolymerization dependent on the concentration of motors on MT. Physically, the processive nature of the motors increases molecular traffic at the microtubule plus end for higher concentrations. This motor blockage initiates a cooperative action resulting in speedy depolymerization, which overly widens the regime of MT shrinkage. Moreover, it is significant to mention here that in contrast to previous study [23], in the proposed framework

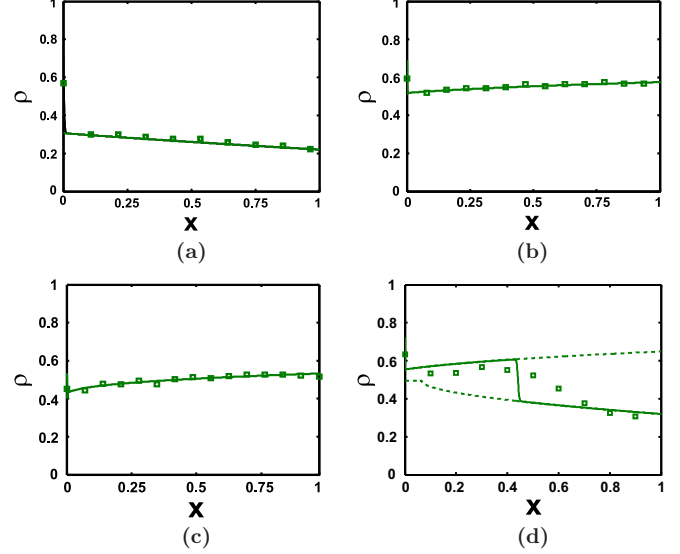


FIG. 6. Density profiles of (a) LD ($\rho < 0.5$), (b) HD ($\rho > 0.5$), (c) LH, (d) S phases with (a) $\alpha = 0.22, \gamma = 0.22$, (b) $\alpha = 0.8, \gamma = 0.23$, (c) $\alpha = 0.35, \gamma = 0.35$, (d) $\alpha = 0.32, \gamma = 0.21$; $N = 1000$, $\omega_D = 0.20$, $c = 100$, $\Omega_a = 5.3 \times 10^{-4}$, $\Omega_d = 7.6 \times 10^{-4}$, and $\delta = 1.1$. Solid and dotted lines denote profiles obtained from Lambert W function while markers (squares) represent the Monte Carlo simulation results. HD and LD profiles are captured by Lambert W branch given in Eqs. (23) and (24) along suitable boundary conditions as discussed in Sec. III, respectively. In (d), solid curve is obtained by solving Eq. (7) numerically.

MT dynamics depends significantly upon the motor concentration.

Further, we examined the effect of increasing modifying factor δ on the system dynamics by means of dotted phase boundaries for $\delta = 1.5$ in Fig. 4. It is noteworthy to mention that as the magnitude of δ increases, no qualitative change in the phase diagram is seen except for shifting of phase boundaries. Moreover, no new phase emerges for higher values of δ in the phase diagram.

In order to understand the system dynamics in steady state, some typical density profiles representing masses of particles progressing along the lattice are displayed in Fig. 6. To validate the theoretical outcomes from continuum mean-field equations, we have included the simulation results as exhibited in Fig. 6. Here, high and low density profiles are obtained by using Eq. (23) along with Eq. (24), respectively. We further obtained full shock profile by solving Eq. (7) with suitable numerical scheme along with two boundary conditions $\rho(0) = \rho_3$ and $\rho(1) = \alpha$. As evident from the Figs. 6(a)–6(d), the theoretical results obtained from mean-field theory using Lambert W function correlates well with simulation results. The visible variations are primarily because of the significant correlations emerging in the system due to strong cooperation among the first three sites, resulting in deviations since the mean-field theory ignores correlations. Similar deficiencies have already been discussed and reported in the literature [34].

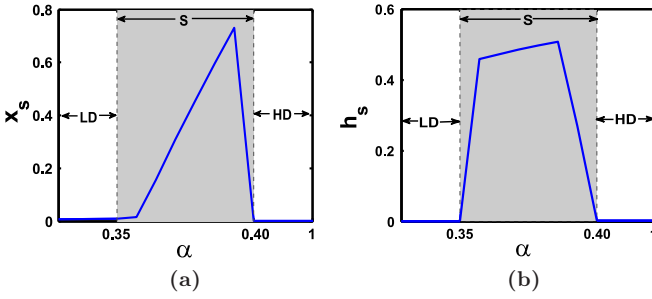


FIG. 7. (a) Shock position, (b) shock height for $\gamma = 0.03$ with $N = 1000$, $\omega_D = 0.20$, $c = 100$, $\Omega_a = 5.3 \times 10^{-4}$, $\Omega_d = 7.6 \times 10^{-4}$, and $\delta = 1.1$. The shaded portion shows magnified region of shock phase.

B. Shock dynamics

The distinctive feature of the proposed system is the appearance of shock which has not been reported in the earlier studies on microtubule length control including both polymerization and depolymerization [38–40]. In contrast to [23], in this study, shock phase emerges for smaller values of c and persists for its higher values as well. We examine the indistinguishable shock entities: shock position (x_s) and shock height (h_s) with respect to α . It is significant to mention here that the shock dynamics is not visualized with respect to concentration since the phase plane changes significantly, resulting in shifting of phases, with varied c (Fig. 4). The shock position is computed by using the constancy of the current across the shock, viz., $\rho_+^2 - \rho_+ = \rho_-^2 - \rho_-$, where $\rho_+ = \lim_{x \rightarrow x_s^+} \rho(x)$ and $\rho_- = \lim_{x \rightarrow x_s^-} \rho(x)$. Figure 7(a) shows the shock position for a fixed γ for varied α . For smaller values of α , until $\alpha \approx 0.35$, we encounter low density phase as exhibited in Fig. 4(b). Later, with an increase in α , when the LD region transits into S phase, shock travels linearly toward right boundary resulting in an upward jump as seen in Fig. 7(a). Further, for $\alpha > 0.4$, on entering the HD region from the S phase [see Fig. 4(b)], downward fall in shock position is observed. The two discontinuities in Fig. 7(a) reveal two phase transitions from LD \rightarrow S and S \rightarrow HD phase, respectively. Moreover, we have also calculated the variations in the shock height ($h_s = \rho_+ - \rho_- = 2\rho_+ - 1$) with respect to α along lines of constant polymerization rate γ . Figure 7(b) shows the height of shock with respect to α along constant γ . For $0.35 < \alpha < 0.41$, h_s jumps discontinuously to a finite value on entering the S region from the LD phase, whereas, at the phase boundary between the HD and S phases, h_s jumps to zero discontinuously. As expected, shock height increases continuously in the S regime.

C. Microtubule length dynamics

To figure out how the system switches between the phases of growth and shrinkage, we consider kymographs of the MT, which exhibit how the MT length and the motor density progress with time. MC simulations show that the MT length varies around a well-defined average value, as depicted in Fig. 8. Specifically, the length dynamics is irregular with alternate switching within elongation and shrinkage feature, in-

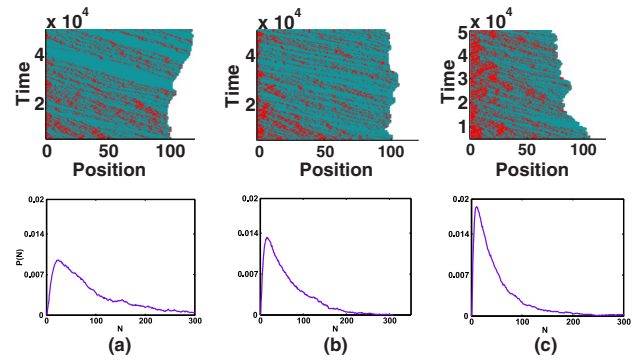


FIG. 8. Effect of motor concentration on kymographs and corresponding length distribution exhibiting the MT dynamics with time for (a) $c = 20$, (b) $c = 50$, (c) $c = 180$ with $N = 100$, $\alpha = 0.15$, $\gamma = 0.16$, $\omega_D = 0.20$, $\Omega_a = 5.3 \times 10^{-4}$, $\Omega_d = 7.6 \times 10^{-4}$, and $\delta = 1.1$ obtained from Monte Carlo simulations. Empty sites are shown in cyan, occupied sites in red. $P(N)$ denotes probability density function for length N . Note that kymographs are plotted by left aligning the lattice.

dicating the dynamic nature of MT. Figures 8(a)–8(c) explore the MT dynamics under the effect of cooperative interactions for a range of motor concentrations $c = 20, 50$, and 180 with the corresponding unimodal length distributions. As expected, MT regulation is directly influenced by motor traffic. For low concentration, hence, for the low density of particles, polymerization predominates because of slow depolymerization [Fig. 8(a)]. With further increase in concentration, we recovered evident interplay between growth and shrinkage phase resulting in an intermediate regime due to the significant impact of depolymerization. Remarkably, during this scenario, we observed intermittent dynamics of MT length with random and frequent switching within growth and shrinkage phase, shown in Fig. 8(b). The observation reveals an interesting outcome of accelerated depolymerization dependent on the concentration of motors on MT. Moreover, when the motor concentration increases to larger values, strong enough depolymerization dynamics to overcome MT growth due to polymerization has been observed, resulting in dominant shrinkage regime [Fig. 8(c)]. The above findings firmly point toward a strong correlation between the depolymerization dynamics and the density of the proteins. Qualitatively, this action can be easily understood from the corresponding length distributions in Figs. 8(a)–8(c). The increasing values of c result in smaller averages, hence accelerated depolymerization. The overall scenario makes instinctive physical perception that the concentration of the motors along MT influence each other, thereby, affect its dynamics crucially in accordance with the flux-dependent shrinkage as revealed in *in vivo* and *in vitro* experiments [22].

Further, to analyze the importance of the interplay between motor traffic and depolymerization dynamics at the MT tip, Fig. 9 gives variation in MT length distribution for the proposed model against varied concentrations. The increase in motor flux initiates mutual cooperation among the particles, hence, dominantly affects the depolymerization rate. Based on the corresponding length distributions, it is evident that

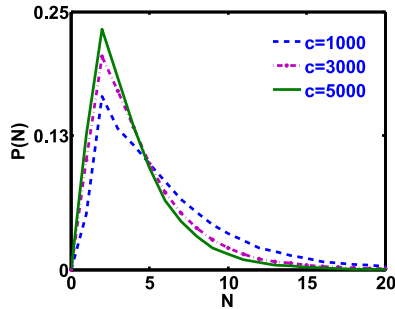


FIG. 9. Effect of the motor concentration on the steady-state length distribution for various values of (a) $c = 1000$, (b) $c = 3000$, (c) $c = 5000$ with $\alpha = 0.8$, $\gamma = 0.15$, $\omega_D = 0.20$, $\Omega_a = 5.3 \times 10^{-4}$, $\Omega_d = 7.6 \times 10^{-4}$, and $\delta = 1.1$ obtained from Monte Carlo simulations.

both average MT length and the distribution width decreases with increase in motor intensity, signifying depolymerization is accelerated with an increase in motor concentration as also observed experimentally [22].

Now, to examine the effect of MT motor concentration on length regulation, we explore the outcomes obtained from our theoretical analysis (MF approximations) for the MT drift velocity, with respect to the polymerization and the depolymerization rates. Figures 10(a) and 10(b) exhibit the regimes of MT growth and shrinkage as a function of polymerization and depolymerization rates with varied concentration by means of a color code. Variation from orange to red color represents the increase in the MT length. The alteration in concentration has generated notable differences for the distinct scenario. The prevailing progression is that the region where MTs shrink is enlarged with an increase in motor traffic. Physically, at high concentrations, on account of the highly processive nature of motors, the flux of molecular traffic at the microtubule plus end increases. Such jamminglike situation initiates a cooperative mechanism resulting in accelerated depolymerization, which drastically widens the regime of MT shrinkage.

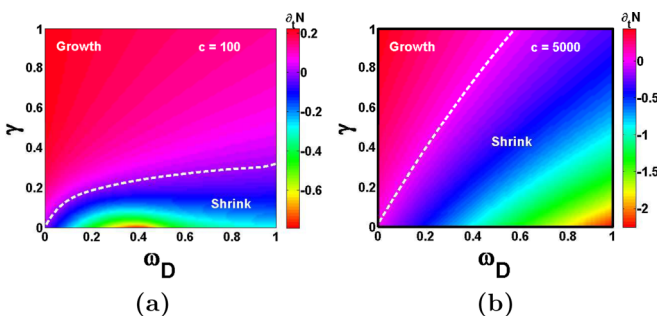


FIG. 10. Drift velocity of the MT tip $\frac{\partial N}{\partial t}$ as a function of the polymerization and depolymerization rates for (a) $c = 100$, (b) $c = 5000$ with $N = 1000$, $\alpha = 0.8$, $\Omega_a = 5.3 \times 10^{-4}$, $\Omega_d = 7.6 \times 10^{-4}$, and $\delta = 1.1$ as obtained from theoretical analysis. Color code ranging from orange to red indicates the magnitude of the drift velocity. Dashed white line indicates where the zero MT velocity as retrieved from the analytical calculations, using Eq. (27).

Further, we take particular interest in analyzing the effect of modifying factor $\delta > 1$ on the system dynamics. In this direction, Figs. 11(a) and 11(b) present the MT length dynamics [Eq. (27)] for varied δ in the controlling parameter space (γ, ω_D) and (α, c) , respectively. Clearly, as anticipated, the observed routine from Fig. 11(a) indicates that the regime where MT shrink is extended with an increase in modifying factor δ . Indeed, as examined from Fig. 11(b), increasing motor traffic on MT due to enhanced concentration and entry rate results in dominating shrinkage domain similar to Fig. 4, which further widens with raised δ on account of accelerated depolymerization. Besides, predominantly to examine the relation between motor flux and depolymerization dynamics, we plot the steady-state current in the α - c plane in Fig. 11(c). As expected, Fig. 11(c) clearly reveals that the lesser current corresponds to more depolymerization. This can be understood as follows. Although increase in the number of particles due to enhanced α and c leads to lesser current on the microtubule on account of highly processive nature of motors, the traffic near the MT tip increases, resulting in accelerated depolymerization as reported in experimental study [22]. It is noteworthy to mention that as evident from Figs. 11(b) and 11(c), drift velocity in the proposed model depends crucially on concentration in contrast to that observed in the previous study [23].

The outcomes of the accomplished model are in accordance with the experimental observations reported in the literature [22]. Our study not only captures the cooperative motor action for depolymerization dynamics at the MT tip, but is also useful to understand the cooperation between the molecular motor and microtubule length dynamics, in general. The overall scenario portraying the interplay between motor traffic and MT kinetic at the plus end provides new theoretical insights into the role of collective mechanism on MT assembly and disassembly dynamics.

VI. SUMMARY AND CONCLUSION

In this work, we investigated how flux-dependent accelerated depolymerization along with particle induced polymerization can result in length control of biological filament network. On a broader perspective, we constructed a stochastic mathematical model capturing the collective mechanism of the plus-end-directed motor traffic undergoing attachment-detachment process on the MT dynamics. The dynamical rules are motivated by well established molecular properties of MT-associated proteins from kinesin family [22]. The effect of the cooperative action is included by modifying the depolymerization rate based on the configuration of two nearest neighboring sites. To explore the system dynamics, mean-field equations in the continuum limit are computed and the resultant analytic solution is expressed in terms of Lambert W functions. The theoretical outcomes are validated by extensively performed Monte Carlo simulations. Additionally, the steady-state dynamics is examined by exploring vital characteristics including phase diagrams, density profiles, phase transitions, and drift velocity.

The phase diagrams are derived in the parameter space of (α, γ) and the influence of cooperative motor action is

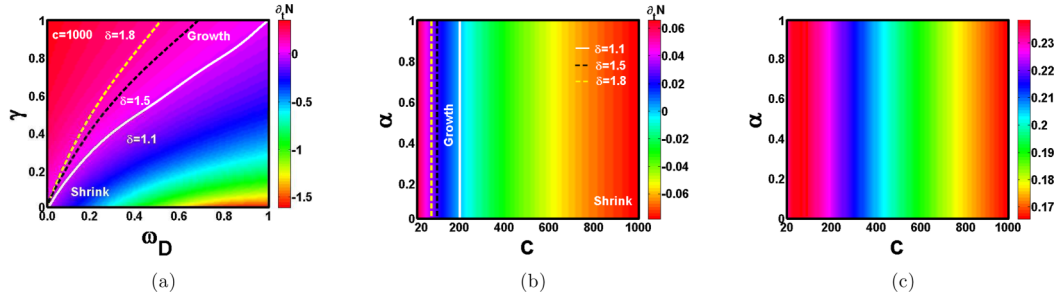


FIG. 11. Effect of modifying factor δ on the system dynamics in (a) (γ, ω_D) parameter space for $\alpha = 0.8$, (b) (α, c) parameter space for $\gamma = 0.22$ as obtained from theoretical analysis with $N = 1000$, $\omega_D = 0.20$, $\Omega_a = 5.3 \times 10^{-4}$, $\Omega_d = 7.6 \times 10^{-4}$, and $\delta = 1.1$. (c) Same parameters as in (b). Color code ranging from orange to red indicates the magnitude of the drift velocity and current in (a), (b), and (c), respectively, for $\delta = 1.1$.

thoroughly investigated. We have categorized the phase diagrams in terms of motor concentration c . Four different steady-state phases have been observed including two new phases, namely, shock phase S and mixed phase LH. Although the LH phase exists only for the intermediate value of c , however, shock persists for all values describing nonmonotonic behavior of phase domains with respect to motor concentration. Moreover, as revealed through theoretical analysis, the existence of these two phases is one of the significant outcomes of the proposed study although these phases have not been reported experimentally and in previous similar studies from literature [35,38,39]. Therefore, we hope that by performing *in vitro* and *in vivo* experiments under well controlled environments where the chosen polymerization and depolymerization processes play an important role, traffic jams by molecular motors might be observed. The presence of shock has strong relevance in the proposed study which can be explained as follows. It reveals that cooperative depolymerization leads to accumulation of motors at plus end, leading to traffic-jam-like situation, thereby making it a significant phenomenon which acts like a bottleneck and affects the motors motility. Additionally, the presence of shock indicates that both polymerization and flux-dependent depolymerization together produce a coexistence region which is a notable feature of such nonequilibrium process. To explore the shock phase further, based on the mean-field approach, we have also analyzed the indistinguishable features of stationary shock including its position and height.

Similar to the outcomes from the experimental studies, our study discloses that the flux of molecular traffic impacts the system dynamics crucially. With increase in the motor concentrations, both qualitative and quantitative crucial topological changes are observed in the phase diagram, due to the appearance and disappearance of existing phases. The critical values of the concentration beyond which a specific phase appears and disappears are also identified. We feel that these critical values of concentration can be utilized by biologists to perform experiments for exploring the effect of collective dynamics on the microtubule length characteristics presented in the proposed system. The complexity of the phase diagram decreases along with an increase in motor concentrations due to enhanced flux on the microtubule. Additionally, increased motor flux due to surged concentration initiates the cooperative action among the motors near the MT

tip resulting in speedy depolymerization as reported in the experimental study [22]. The interplay between motor flux and depolymerization processes at the MT plus end results in robust correlations between the depolymerization dynamics and density profiles of depolymerases.

To study the fluctuations in the microtubule length, based on the Monte Carlo simulations, we provided kymographs of the microtubule dynamics along with length distribution depicting the translations between the phases of growth and shrinkage. As anticipated, MT regulation is directly controlled by motor traffic. For the low density of particles, polymerization predominates, while for its larger values, dominant shrinkage regime is discovered resulting in large fluctuations in the MT length. However, the overall microtubule length remains almost constant with only small fluctuations in the case of intermediate values of motor flux. The above findings capture correlations between the depolymerization dynamics and the density of the proteins. Therefore, the proposed model provides a verification of principle that spatial dependencies in the magnification and diminished rates of microtubules, which emerge from proteins transport in this case, can result in an average filament length.

We additionally studied the impact of motor concentration and modifying factor on the MT drift velocity for the proposed scenario. As expected, the increase in concentrations enlarged the region where MTs shrink and reveals an interesting outcome of accelerated depolymerization dependent on the flux of motors near the tip on the MT similar to those observed experimentally [22]. We found the motor concentration which is required to reach a steady-state microtubule length. In case of less number of motors, the chosen depolymerization process cannot be sufficiently speedy to balance the intrinsic polymerization. Moreover, the steady-state lattice length relies crucially on the motor flux, implying that this process of length regulation needs hard control of the total number of motors to regulate successfully.

The proposed work is an attempt to provide natural means to gain deeper insight into the steady-state properties of collective dynamics on intracellular transport by motors, in particular, the interactions between the individual motors and the MT tip playing a crucial role in length regulation. The theoretical framework developed here is not only limited to a specific motor family which collaborates with microtubules, but also can be utilized for any kind of proteins which control

the dynamics of filament ends. Similarly, our findings might be useful in understanding other enzymatic processes forming a nonequilibrium system and are not restricted to only microtubules and their associated motors. It is worthwhile to mention that our results are not very sensitive with respect to chosen parameters, therefore, small perturbations in their values do not alter the steady-state system properties.

Further, the progression of molecular motors along multiple microtubules accompanied by lane switching stimulates the curiosity to explore the role of coupling on microtubule length dynamics. Therefore, future study aims to analyze the interplay between the spontaneous polymerization and motor induced depolymerization along several coupled microtubules.

APPENDIX A

The model studied in main text does not include the polymerization and depolymerization processes when the MT tip is empty. So here, in addition to dynamical rules presented in the main text, we incorporate the remaining processes to visualize the combined effect on the phase diagram of the proposed model as follows. If MT tip is empty, polymerization (depolymerization) takes place with rate γ^* (ω_{D^*}), respectively. The resulting equations for $i \geq 4$ (bulk of lattice) then read as

$$\begin{aligned} \frac{d\langle\tau_i\rangle}{dt} = & \langle\tau_{i+1}(1-\tau_i)\rangle - \langle\tau_i(1-\tau_{i-1})\rangle + c\omega_a\langle 1-\tau_i\rangle \\ & - \omega_d\langle\tau_i\rangle + \gamma\langle\tau_i(\tau_{i-1}-\tau_i)\rangle \\ & + \gamma^*\langle(1-\tau_i)(\tau_{i-1}-\tau_i)\rangle \\ & + \omega_D[\delta\langle\tau_1\tau_2(\tau_{i+1}-\tau_i)\rangle + \delta^2\langle\tau_1\tau_2\tau_3(\tau_{i+1}-\tau_i)\rangle] \\ & + \omega_{D^*}\langle(1-\tau_i)(\tau_{i+1}-\tau_i)\rangle. \end{aligned} \quad (A1)$$

Here, capturing the interplay between the MT tip and motors, terms corresponding to γ^* and ω_{D^*} exemplify the role of polymerization and depolymerization dynamics in the absence of molecular motor, respectively. The resulting particle density at the sites $i = 1, 2$, and 3 in the comoving frame of the tip can be computed as

$$\begin{aligned} \frac{d\langle\tau_1\rangle}{dt} = & \langle\tau_2(1-\tau_1)\rangle - \gamma\langle\tau_1\rangle - \gamma^*\langle\tau_1\rangle - \omega_{D_1}\langle\tau_1\rangle \\ & + \omega_{D^*}\langle(1-\tau_1)\tau_2\rangle, \\ \frac{d\langle\tau_2\rangle}{dt} = & \langle\tau_3(1-\tau_2)\rangle - \langle\tau_2(1-\tau_1)\rangle - \gamma\langle\tau_1\tau_2\rangle \\ & - \gamma^*\langle(1-\tau_1)\tau_2\rangle + c\omega_a\langle 1-\tau_2\rangle \\ & - \omega_d\langle\tau_2\rangle + \delta\omega_D\langle\tau_1\tau_2\tau_3\rangle - \delta\omega_D\langle\tau_1\tau_2\rangle \\ & + \omega_{D^*}\langle(1-\tau_1)\tau_3\rangle - \omega_{D^*}\langle(1-\tau_1)\tau_2\rangle, \\ \frac{d\langle\tau_3\rangle}{dt} = & \langle\tau_4(1-\tau_3)\rangle - \langle\tau_3(1-\tau_2)\rangle + \gamma\langle\tau_1\tau_2\rangle - \gamma\langle\tau_1\tau_3\rangle \\ & + \gamma^*\langle(1-\tau_1)\tau_2\rangle - \gamma^*\langle(1-\tau_1)\tau_3\rangle + c\omega_a\langle 1-\tau_3\rangle \\ & - \omega_d\langle\tau_3\rangle + \delta\omega_D\langle\tau_1\tau_2\tau_4\rangle - \delta\omega_D\langle\tau_1\tau_2\tau_3\rangle \\ & + \delta^2\omega_D\langle\tau_1\tau_2\tau_3\tau_4\rangle - \delta^2\omega_D\langle\tau_1\tau_2\tau_3\rangle \\ & + \omega_{D^*}\langle(1-\tau_1)\tau_4\rangle - \omega_{D^*}\langle(1-\tau_1)\tau_3\rangle. \end{aligned} \quad (A2)$$

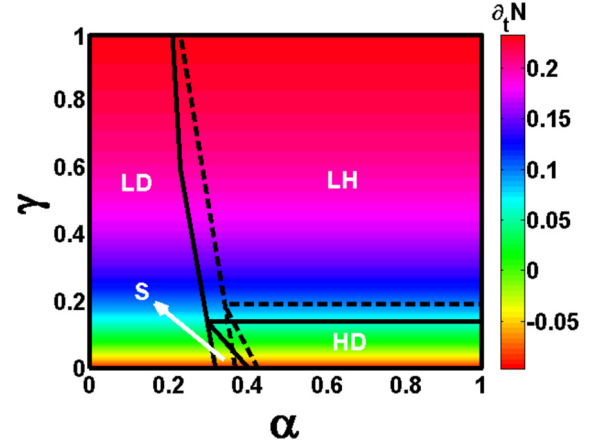


FIG. 12. Phase diagrams for $c = 100$, $N = 1000$, $\omega_D = 0.2$, $\Omega_a = 5.3 \times 10^{-4}$, $\Omega_d = 7.6 \times 10^{-4}$, $\gamma^* = 0.2$, and $\omega_{D^*} = 0.1$. Solid lines denote phase transition for $\delta = 1.1$, while dotted lines are those obtained for $\delta = 1.5$. Color code running from orange to red represents the transition from shrinkage to growth phase as calculated from Eq. (A3) for $\delta = 1.1$.

Similarly, rate of change in lattice length can be calculated as

$$\begin{aligned} \frac{\partial N}{\partial t} = & \gamma\rho_1 + \gamma^*(1-\rho_1) - \delta\omega_D\rho_1\rho_2 - \delta^2\omega_D\rho_1\rho_2\rho_3 \\ & - \omega_{D^*}(1-\rho_1). \end{aligned} \quad (A3)$$

Based on the similar mathematical techniques as discussed in Sec. III, we solved the above systems of equations and calculated the phase diagram for $\gamma^* = 0.20$ and $\omega_{D^*} = 0.1$ [22] shown in Fig. 12. The additional processes do not affect system dynamics significantly and no qualitative changes are observed in the phase diagram. As evident from the figure, we obtained the same four steady-state phases which were observed earlier, ignoring the additional polymerization and depolymerization processes. Besides, an increase in γ^* only leads to shifting of phase boundaries and does not produce any new phase.

APPENDIX B

Here for better insight, we discuss the derivation for the solution of Eq. (14). In this direction, from Eq. (13), we can obtain

$$\rho = \frac{c\Omega_a + \Omega_d}{2} = \frac{1 - \gamma\rho_1 + \delta\omega_D\rho_1\rho_2(1 + \delta\rho_3)}{2} \quad (B1)$$

or

$$\frac{d\rho}{dx} = -B. \quad (B2)$$

Integrating the above equation,

$$\rho(x) = -Bx + \text{const.} \quad (B3)$$

Applying boundary conditions $\rho(0) = \rho_3$ and $\rho(1) = \alpha$ which are responsible for high and low density phases, respectively, results in

$$\rho(x) = \rho_3 - Bx, \quad (B4)$$

$$\rho(x) = \alpha + B(1-x). \quad (B5)$$

Combining the above solutions, we obtain the solution as given in Eq. (15).

APPENDIX C

For further clarity, we incorporate the detailing of Eq. (18) as derived from Eq. (17). Equation (17) reads as

$$\partial_x \sigma(x) + \partial_x \ln |\sigma(x)| = -\frac{\Omega_d(K+1)^2}{H}. \quad (C1)$$

We can also write above equation in following way:

$$\partial_x \ln |\exp[\sigma(x)]| + \partial_x \ln |\sigma(x)| = -\frac{\Omega_d(K+1)^2}{H}, \quad (C2)$$

$$\partial_x \ln |\sigma(x) \exp[\sigma(x)]| = -\frac{\Omega_d(K+1)^2}{H}. \quad (C3)$$

Integrating from x_0 to x leads to

$$\ln |\sigma(x) \exp[\sigma(x)]| = \ln |\sigma(x_0) \exp[\sigma(x_0)]| - \frac{\Omega_d(K+1)^2}{H}(x-x_0), \quad (C4)$$

$$|\sigma(x)| \exp[\sigma(x)] = |\sigma(x_0)| \exp[\sigma(x_0)] - \frac{\Omega_d(K+1)^2}{H}(x-x_0). \quad (C5)$$

APPENDIX D

We provide an alternative approach to determine the solutions of Eq. (12). Integrating Eq. (12), we have

$$2(\rho_b - \rho) + (1 - \gamma \rho_1 + \delta \omega_D \rho_1 \rho_2 (1 + \delta \rho_3) - \frac{2c\Omega_a}{c\Omega_a + \Omega_d}) \times \log \left[\frac{\rho(c\Omega_a + \Omega_d) - c\Omega_a}{\rho_b(c\Omega_a + \Omega_d) - c\Omega_a} \right] = (c\Omega_a + \Omega_d)(x - x_b), \quad (D1)$$

leading to

$$\frac{\rho(c\Omega_a + \Omega_d) - c\Omega_a}{\rho_b(c\Omega_a + \Omega_d) - c\Omega_a} = \exp(Q) \quad (D2)$$

with $Q = \frac{(c\Omega_a + \Omega_d)(x - x_b) - 2(\rho_b - \rho)}{1 - \gamma \rho_1 + \delta \omega_D \rho_1 \rho_2 (1 + \delta \rho_3) - \frac{2c\Omega_a}{c\Omega_a + \Omega_d}}$. Here, x_b represents the position of the boundary and ρ_b denotes the boundary density. $x_b = 0$ signifies left boundary while $x_b = 1$ represents right end of the lattice. Note that when density profile satisfies the condition at the left boundary, $x_b = 0$, then the corresponding boundary density is the density at site 3, i.e., $\rho(0) = \rho_3$. The obtained profile corresponds to high density phase. Similarly, for the density profile satisfying the boundary condition at the other end, $x_b = 1$, the observed boundary density from Eq. (11) results in $\rho(1) = \alpha$. This density profile signifies low density phase. The shock location can be obtained by equating the current from low and high density phases. It is to be noted that this technique provides implicit solution, whereas one can extract explicit density profiles using Lambert W function as discussed in the main text. Moreover, as expected, the density profiles obtained using this technique exactly overlap with those observed from Lambert W function, thus validating our theoretical outcomes as well.

-
- [1] H. Lodish, A. Berk, S. L. Zipursky, P. Matsudaira, D. Baltimore, J. Darnell *et al.*, *Molecular Cell Biology* (WH Freeman, New York, 1995), Vol. 3.
- [2] J. E. Rothman, *Nature (London)* **372**, 55 (1994).
- [3] J. Howard and A. A. Hyman, *Nature (London)* **422**, 753 (2003).
- [4] F. Jülicher and J. Prost, *Phys. Rev. Lett.* **75**, 2618 (1995).
- [5] L. Scharrel, R. Ma, R. Schneider, F. Jülicher, and S. Diez, *Biophys. J.* **107**, 365 (2014).
- [6] R. Lipowsky, Y. Chai, S. Klumpp, S. Liepelt, and M. J. Müller, *Physica A (Amsterdam)* **372**, 34 (2006).
- [7] R. Lipowsky, J. Beeg, R. Dimova, S. Klumpp, and M. J. Müller, *Physica E (Amsterdam)* **42**, 649 (2010).
- [8] R. Mallik and S. P. Gross, *Curr. Biol.* **14**, R971 (2004).
- [9] D. J. Sharp, G. C. Rogers, and J. M. Scholey, *Nature (London)* **407**, 41 (2000).
- [10] U. S. Eggert, T. J. Mitchison, and C. M. Field, *Annu. Rev. Biochem.* **75**, 543 (2006).
- [11] J. L. Ross, M. Y. Ali, and D. M. Warshaw, *Curr. Opin. Cell Biol.* **20**, 41 (2008).
- [12] J. Howard and A. A. Hyman, *Curr. Opin. Cell Biol.* **19**, 31 (2007).
- [13] J. G. Cueva, J. Hsin, K. C. Huang, and M. B. Goodman, *Curr. Biol.* **22**, 1066 (2012).
- [14] T. Mitchison and M. Kirschner, *Nature (London)* **312**, 237 (1984).
- [15] G. Goshima, R. Wollman, N. Stuurman, J. M. Scholey, and R. D. Vale, *Curr. Biol.* **15**, 1979 (2005).
- [16] W. F. Marshall, H. Qin, M. R. Brenni, and J. L. Rosenbaum, *Mol. Biol. Cell* **16**, 270 (2005).
- [17] R. Walker, E. O'Brien, N. Pryer, M. Soboeiro, W. Voter, H. Erickson, and E. Salmon, *J. Cell Biol.* **107**, 1437 (1988).
- [18] T. L. Hill, *Proc. Natl. Acad. Sci. USA* **81**, 6728 (1984).
- [19] D. M. Suter and K. E. Miller, *Prog. Neurobiol.* **94**, 91 (2011).
- [20] V. Varga, J. Helenius, K. Tanaka, A. A. Hyman, T. U. Tanaka, and J. Howard, *Nat. Cell Biol.* **8**, 957 (2006).
- [21] G. Drewes, A. Ebneith, and E.-M. Mandelkow, *Trends Biochem. Sci.* **23**, 307 (1998).
- [22] V. Varga, C. Leduc, V. Bormuth, S. Diez, and J. Howard, *Cell* **138**, 1174 (2009).
- [23] L. Reese, A. Melbinger, and E. Frey, *Biophys. J.* **101**, 2190 (2011).
- [24] M. K. Gardner, D. C. Bouck, L. V. Paliulis, J. B. Meehl, E. T. O'Toole, J. Haase, A. Soubry, A. P. Joglekar, M. Winey, E. D. Salmon *et al.*, *Cell* **135**, 894 (2008).
- [25] C. T. MacDonald, J. H. Gibbs, and A. C. Pipkin, *Biopolymers* **6**, 1 (1968).

- [26] D. Chowdhury, L. Santen, and A. Schadschneider, *Phys. Rep.* **329**, 199 (2000).
- [27] M. Evans, D. Foster, C. Godreche, and D. Mukamel, *J. Stat. Phys.* **80**, 69 (1995).
- [28] A. B. Kolomeisky, G. M. Schütz, E. B. Kolomeisky, and J. P. Straley, *J. Phys. A: Math. Gen.* **31**, 6911 (1998).
- [29] M. R. Evans, R. Juhasz, and L. Santen, *Phys. Rev. E* **68**, 026117 (2003).
- [30] A. K. Gupta and I. Dhiman, *Phys. Rev. E* **89**, 022131 (2014).
- [31] C. Erlenkämper and K. Kruse, *Phys. Biol.* **6**, 046016 (2009).
- [32] E. Reithmann, L. Reese, and E. Frey, *Phys. Rev. Lett.* **117**, 078102 (2016).
- [33] S. Muhuri, *Europhys. Lett.* **101**, 38001 (2013).
- [34] K. Sugden and M. Evans, *J. Stat. Mech.: Theory Exp.* (2007) P11013.
- [35] C. Arita, A. Lück, and L. Santen, *J. Stat. Mech.: Theory Exp.* (2015) P06027.
- [36] M. Ebbinghaus and L. Santen, *Biophys. J.* **100**, 832 (2011).
- [37] G. A. Klein, K. Kruse, G. Cuniberti, and F. Jülicher, *Phys. Rev. Lett.* **94**, 108102 (2005).
- [38] L. Reese, A. Melbinger, and E. Frey, *Interface Focus* **4**, 20140031 (2014).
- [39] A. Melbinger, L. Reese, and E. Frey, *Phys. Rev. Lett.* **108**, 258104 (2012).
- [40] D. Johann, C. Erlenkämper, and K. Kruse, *Phys. Rev. Lett.* **108**, 258103 (2012).
- [41] L. Hough, A. Schwabe, M. A. Glaser, J. R. McIntosh, and M. Betterton, *Biophys. J.* **96**, 3050 (2009).
- [42] C. Appert-Rolland, S. Klein, M. Ebbinghaus, and L. Santen, in *Proceedings of the Asia-Pacific Econophysics Conference 2016- Big Data Analysis and Modeling toward Super Smart Society (APEC-SSS2016)* (The Physical Society of Japan, Japan, 2017), p. 011001.
- [43] A. Akhmanova and C. C. Hoogenraad, *Curr. Biol.* **25**, R162 (2015).
- [44] Y. Chen and W. O. Hancock, *Nat. Commun.* **6**, 8160 (2015).
- [45] A. K. Gupta, *J. Stat. Phys.* **162**, 1571 (2016).
- [46] A. Parmeggiani, T. Franosch, and E. Frey, *Phys. Rev. Lett.* **90**, 086601 (2003).
- [47] R. M. Corless, G. H. Gonnet, D. E. Hare, D. J. Jeffrey, and D. E. Knuth, *Adv. Comput. Math.* **5**, 329 (1996).